



CHALMERS

Chalmers Publication Library

Analysis of structurally sensitive loss in GaN-based VCSEL cavities and its effect on modal discrimination

This document has been downloaded from Chalmers Publication Library (CPL). It is the author's version of a work that was accepted for publication in:

Optics Express (ISSN: 1094-4087)

Citation for the published paper:

Hashemi, S. ; Bengtsson, J. ; Gustavsson, J. (2014) "Analysis of structurally sensitive loss in GaN-based VCSEL cavities and its effect on modal discrimination". Optics Express, vol. 22(1), pp. 411-426.

<http://dx.doi.org/10.1364/OE.22.000411>

Downloaded from: <http://publications.lib.chalmers.se/publication/191636>

Notice: Changes introduced as a result of publishing processes such as copy-editing and formatting may not be reflected in this document. For a definitive version of this work, please refer to the published source. Please note that access to the published version might require a subscription.

Chalmers Publication Library (CPL) offers the possibility of retrieving research publications produced at Chalmers University of Technology. It covers all types of publications: articles, dissertations, licentiate theses, masters theses, conference papers, reports etc. Since 2006 it is the official tool for Chalmers official publication statistics. To ensure that Chalmers research results are disseminated as widely as possible, an Open Access Policy has been adopted. The CPL service is administrated and maintained by Chalmers Library.

(article starts on next page)

Analysis of structurally sensitive loss in GaN-based VCSEL cavities and its effect on modal discrimination

Ehsan Hashemi,^{1,*} Jörgen Bengtsson,¹ Johan Gustavsson,¹
Martin Stattin,¹ Gatien Cosendey,² Nicolas Grandjean,² and
Åsa Haglund¹

¹Photonics Laboratory, Department of Microtechnology and Nanoscience,
Chalmers University of Technology, SE-41296 Gothenburg, Sweden

²Laboratory of Advanced Semiconductors for Photonics and Electronics, Institute of
Condensed Matter Physics, École Polytechnique Fédérale de Lausanne (EPFL), CH-1015
Lausanne, Switzerland

*ehsan.hashemi@chalmers.se

Abstract: Lateral loss causes optical energy to leave the laser cavity in the transverse, lateral, direction, and is sometimes neglected to simplify the numerical simulations. However, in contrast to outcoupling and absorption losses, we show that the lateral loss can change drastically with only nanometer-sized changes of the cavity structure, from being virtually zero to becoming the major source of cavity loss, since the cavity becomes antiguiding. This can be explained as the opening of a channel of efficient resonant lateral leakage of optical power at a certain oblique propagation angle. A number of different realizations of current apertures and top mirror designs in GaN-based VCSEL cavities, which have been suggested for realization of microcavity lasers emitting in the blue wavelength range, are simulated. Many of these are shown to lead to unintentional antiguiding, which can more than double the threshold gain for lasing. Notably, for strong enough antiguiding the resonant lateral leakage decreases so that the threshold gain values might again be tolerable. This regime has been suggested for robust single-mode operation since earlier predictions, building on analogies with slab waveguides, hinted at a very strong suppression of higher order modes. However, our simulations indicate that for the VCSEL cavities the derived formulas grossly overestimate the modal discrimination.

© 2014 Optical Society of America

OCIS codes: (050.0050) Diffraction and gratings; (140.3948) Microcavity devices; (140.7260) Vertical cavity surface emitting lasers.

References and links

1. G. Cosendey, A. Castiglia, G. Rossbach, J. F. Carlin, and N. Grandjean, "Blue monolithic AlInN-based vertical cavity surface emitting laser diode on free-standing GaN substrate," *Appl. Phys. Lett.* **101**(15), 151113 (2012).
2. C. Holder, J. S. Speck, S. P. DenBaars, S. Nakamura, and D. Feezell, "Demonstration of nonpolar GaN-based vertical-cavity surface-emitting lasers," *Appl. Phys. Expr.* **5**, 092104 (2012).
3. T. Onishi, O. Imafuji, K. Nagamatsu, M. Kawaguchi, K. Yamanaka, and S. Takigawa, "Continuous wave operation of GaN vertical cavity surface emitting lasers at room temperature," *IEEE J. Quantum Electron.* **48**(9), 1107–1112 (2012).
4. D. Kasahara, D. Morita, T. Kosugi, K. Nakagawa, J. Kawamata, Y. Higuchi, H. Matsumura, and T. Mukai, "Demonstration of blue and green GaN-based vertical-cavity surface-emitting lasers by current injection at room temperature," *Appl. Phys. Expr.* **4**, 072103 (2011).

5. T-C. Lu, S-W. Chen, T-T. Wu, P-M. Tu, C-K. Chen, C-H. Chen, Z-Y. Li, H-C. Kuo and S-C. Wang, "Continuous wave operation of current injected GaN vertical cavity surface emitting lasers at room temperature," *Appl Phys. Lett.* **97**(7), 071114 (2010).
6. E. Hashemi, J. Gustavsson, J. Bengtsson, M. Stattin, G. Cosendey, N. Grandjean, and Å. Haglund, "Engineering the lateral optical guiding in gallium nitride-based vertical-cavity surface-emitting laser cavities to reach the lowest threshold gain," *Jap. J. Appl. Phys.* **52**, 08JG04 (2013).
7. J. Piprek and S. Li, "GaN-based VCSELs: Analysis of internal device physics and performance limitations," *Proc. SPIE* **7602**, 760217 (2010).
8. Y. Higuchi, K. Omae, H. Matsumura, and T. Mukai, "Room-temperature cw lasing of a GaN-based vertical-cavity surface-emitting laser by current injection," *Appl. Phys. Expr.* **1**, 121102 (2008).
9. W. Nakwaski, T. Czyszanowski, and R. P. Sarzala, *Nitride Semiconductor Devices: Principles and Simulation*, J. Piprek, ed. (Wiley, 2007).
10. J. S. Gustavsson, J. Vukusic, J. Bengtsson, and A. Larsson, "A comprehensive model for the modal dynamics of vertical-cavity surface-emitting lasers," *IEEE J. Quantum Electron.* **38**(2), 203–212 (2002).
11. J. Bengtsson, J. Gustavsson, Å. Haglund, A. Larsson, A. Bachmann, K. Kashani-Shirazi, and M.-C. Amann, "Diffraction loss in long-wavelength buried tunnel junction VCSELs analyzed with a hybrid coupled-cavity transfer-matrix model," *Opt. Express* **16**(25), 20789–20802 (2008).
12. T. Czyszanowski, M. Wasiak, R. P. Sarzala, and W. Nakwaski, "Exactness of simplified scalar optical approaches in modeling a threshold operation of possible nitride vertical-cavity surface-emitting lasers," *Phys. Stat. Sol. A* **204**(10), 3562–3573 (2007).
13. R. Sarzala, T. Czyszanowski, M. Wasiak, M. Dems, L. Piskorski, W. Nakwaski, and K. Panajotov, "Numerical self-consistent analysis of VCSELs," *Adv. Opt. Technol.* **2012**, ID 689519 (2012).
14. G. R. Hadley, "Effective index model for vertical-cavity surface-emitting lasers," *Opt. Lett.* **20**(13), 1483–1485 (1995).
15. J. W. Goodman, *Introduction to Fourier Optics* (McGraw-Hill, 1996).
16. R. Butté, G. Christmann, E. Feltn, A. Castiglia, J. Levrat, G. Cosendey, A. Altoukhov, J. F. Carlin, and N. Grandjean, "Room temperature polariton lasing in III-nitride microcavities: a comparison with blue GaN-based vertical cavity surface emitting lasers," *Proc. SPIE* **7216**, 721619 (2009).
17. S. C. Wang, T. C. Lu, and H. C. Kuo, "Recent advances on CW current injection blue VCSELs," *Proc. SPIE* **8276**, 827607 (2012).
18. B. S. Cheng, Y. L. Wu, T. C. Lu, C. H. Chiu, C. H. Chen, P. M. Tu, H. C. Kuo, S. C. Wang, and C. Y. Chang, "High Q microcavity light emitting diodes with buried AlN current apertures," *Appl. Phys. Lett.* **99**(4), 041101 (2011).
19. M. Ohya, K. Fukuda, I. Masumoto, S. Kohmoto, K. Naniwae, M. Yamada, M. Matsudate, T. Tsukuda, T. Akagawa, and C. Sasaoka, "High-power operation of inner-stripe GaN-based blue-violet laser diodes," *Proc. SPIE* **6485**, 648505 (2007).
20. W. S. Tan, K. Takahashi, V. Bousquet, A. Ariyoshi, Y. Tsuda, M. Ohta, and M. Kauer, "Blue-violet inner stripe laser diodes using lattice matched AlInN as current confinement layer for high power operation," *Appl. Phys. Expr.* **2**, 112101 (2009).
21. R. W. H. Engelman and D. Kerps, "Leaky modes in active three-layer slab waveguides," *IEE Proc.* **127**(6), 330–336 (1980).
22. D. Zhou and L. J. Mawst, "High-power single-mode antiresonant reflecting optical waveguide-type vertical-cavity surface-emitting lasers," *IEEE J. Quantum Electron.* **38**(12), 1599–1606 (2002).

1. Introduction

Gallium-nitride (GaN)-based light emitters are now key components in general lighting applications and high-density optical data storage. For the latter application, lasers of edge-emitting type are used, which is the only commercially available laser in this material system. The realization of a surface-emitting laser, such as the vertical-cavity surface-emitting laser (VCSEL), would provide a laser with several advantages such as low threshold current, ease to integrate into two-dimensional (2D) arrays, low-divergent circular output beam and possibility for mass fabrication at low cost. Such a laser would be of great interest, e.g., for applications within the fields of high-resolution laser printing, medical diagnosis and bio-sensing. So far, five groups have demonstrated lasing from electrically pumped GaN-based VCSELs [1–5], three of which have achieved continuous operation and two pulsed operation, but the performance characteristics – in terms of output power, threshold current and lifetime – are still very poor compared to those of the more mature gallium-arsenide (GaAs)-based VCSELs with emission in the infrared

wavelength region. Some of the major challenges with the practical realization of GaN-based VCSELs are to achieve high reflectivity broadband distributed Bragg-reflector (DBR) structures in combination with accurate cavity length control, and to achieve current confinement and homogeneous current injection across the active region without introducing too high optical losses. To realize current confinement and homogeneous current injection a dielectric current aperture has been used – a layer of dielectric material with a hole in the center onto which a transparent conductive layer (indium-tin-oxide, ITO) and the dielectric layers of the DBR have been deposited. Because of the hole in the current aperture, this approach leads to a structural depression (towards the active region) of the deposited layers above the hole. We have previously shown that this type of structure has an antiguiding effect, i.e. it tends to make the effective refractive index larger in the peripheral region than in the region closest to the optical axis [6]. This can balance or even outweigh the naturally occurring guiding effect of the current aperture, which normally is dielectric (lower index) in the periphery whereas the hole is filled, at least partly, with a higher-index material. Our previous study showed that the net guiding effect is very precisely described by the effective index, as calculated with a computationally efficient 2D method. Using also a comprehensive 3D method we could calculate the threshold gains for different realizations of GaN-based VCSEL cavities, and it was found that the sudden jump from low to high threshold gains occurred very precisely when the effective index difference between the peripheral and central part of the cavity changes sign. In this paper, we focus on the in-depth analysis of these results and their explanation. We identify and calculate the different contributions to the cavity loss, particularly the lateral loss, which is the optical power loss caused by transport out of the cavity in the transverse direction, with its extreme sensitivity to the cavity structure. We also perform the simulations for the first higher order mode, with no assumptions of what this mode may look like, only that it is orthogonal to the fundamental mode. The thorough loss analysis of the fundamental and first higher order modes finally makes it possible to scrutinize previous claims about the strong discrimination of higher order modes in antiguided cavities.

Numerical simulations of GaN-based VCSELs are complicated because of the detailed structures and a remaining uncertainty regarding both values for several material parameters as well as the importance of phenomena such as the strong self-polarization in GaN-based materials. In [7] two experimentally reported GaN-based VCSELs, including the first room-temperature emitting device from Nichia Corporation [8], were numerically simulated retrospectively. These devices did not have a current aperture, and the main limitations to the performance were found to be electrical, particularly the current crowding, leading to lower threshold currents for higher order modes than for the fundamental mode. A similar multiphysical numerical analysis of GaN-based VCSELs was described in [9]. Here, a device with a tunnel junction was suggested to achieve a more laterally uniform current injection. In this case higher order modes were strongly discriminated when the device heating was low, presumably indicating operation in the antiguiding regime where this behavior is typical, as will be demonstrated. However, the recent interest in GaN-based VCSELs using current apertures makes it important to study their unique optical guiding properties. On one hand there is the dielectric current aperture and the associated radial confinement of the quantum-well region with positive gain, contributing to index guiding and gain guiding. On the other hand there is the change in the topography of the top mirror, as a result of the creation of the current aperture, which often seems to contribute to antiguiding. Since the performance can be dramatically changed for a minimal structural change it is crucial to be aware of the guiding nature of a proposed dielectric-aperture VCSEL. This work highlights this importance for a large number of proposed structures, explains the physical processes underlying the sensitivity of the performance on structure, and its role for stable fundamental-mode operation. For this purpose we want to isolate the structural

dependence of the optical properties from effects of carrier injection and heating, so we do not consider any temperature gradients and use the threshold gain in the quantum wells, rather than the threshold current, as a measure of how easily lasing is achieved in a certain structure.

In this paper, the next section will explain the numerical methods, particularly the 3D method which is the basis of our investigations of threshold gain and loss mechanisms. The threshold gains and loss contributions in the different cavities are shown in Section 3, with a discussion on how these can be explained in Section 4. Finally, in Section 5 we analyze the behaviour of the first higher order mode in these cavities.

2. Numerical simulation methods and loss analysis

For the numerical analysis two different simulation models are used, which will be referred to as the 2D method and the 3D method. The 2D method is used to extract the effective index difference, Δn_{eff} , between the periphery and the central part of the VCSEL cavity [10]. In some cases, the 2D method can also be used to estimate the threshold gain, but since it cannot account for lateral loss it cannot be used for antiguided cavities, nor for strongly guided cavities with significant diffraction loss. Therefore the 3D method is used for all cavities to extract the threshold gain and the data for the loss analysis. A version of the 3D method was used previously in a study of lateral loss in cavity structures simple enough to allow simulation also with a profoundly different method, based on the finite element method. The two methods were then found to agree very well [11].

A similar dual-method approach is taken in [12, 13] where the optical modeling of GaN-based VCSEL cavities is discussed in detail and a strongly simplified scalar approach is compared with a vectorial method. The scalar method is almost identical with our 2D method, and is based on the effective index or effective frequency method [14], which assumes a moderate refractive index contrast so that the optical field is separable in the spatial coordinates in such a way that the wave equation can be reduced to a pair of almost one-dimensional equations. It is shown in [12, 13] that the simplified scalar method and the rigorous vectorial method agree remarkably well in cases where diffraction losses are negligible. The vectorial method is very similar to our 3D method in the consideration of the structure and the cavity field. In both cases the numerical structure is divided into layers within which the refractive index is constant in the longitudinal direction, and in each layer there is one forward- and one backward travelling 2D field. However, because of the near-paraxial propagation the 3D method still treats the intracavity field as a scalar, but it is much more accurate than the effective index method since no field separability or low index contrast is assumed, and diffraction losses are accurately accounted for. Naturally, the more realistic field representation makes it much more computationally demanding than the effective index method.

In the 3D method the layers in the cavity act as coupled subcavities. As mentioned, each subcavity is a segment of the cavity in which there is no variation of the structure in the longitudinal direction, see Fig. 1 for a part of the VCSEL cavity with a few subcavities indicated. In the subcavity, which can have a structural variation in the lateral (transverse) direction, the fields propagating towards right (top) and left (bottom), respectively, are defined at both interfaces to its neighboring subcavities. In total, thus, four two-dimensional, i.e. (x,y) -variant, fields are used for each subcavity. In one iteration of the numerical algorithm, the two fields directed into the subcavity from either interface are propagated through the subcavity to the other interface with a beam-propagation method (BPM), which is a stepwise propagation using the non-paraxial free-space angular spectrum method with a correction in each step for the laterally varying refractive index in the subcavity [15]. The two propagated fields thus become the two fields directed out of the cavity. These two fields, and the corresponding from the neighboring subcavities are then used with the Fresnel equations to update the inward-directed fields by

transmission through and reflection from the subcavity interfaces. Moreover, in each iteration there is also an analysis of the optical cavity field at some predetermined position in the cavity, which compares the amplitude and phase of the field with that obtained in the previous iteration. Based on this analysis, the wavelength and gain in the quantum wells (QWs) are adjusted towards increasing repeatability of the field amplitude and phase between the iterations, thus strictly enforcing the lasing conditions and enabling a direct read-out of the lasing wavelength and threshold gain once the parameters of the optical field have stabilized. The inset in Fig. 1 shows a typical iterative behavior of the dynamically adjusted values for the QW gain. In general, 15000–50000 iterations are used for each simulation; this value depends on the cavity structure and also somewhat on the starting field, which is a random 2D field distribution in one of the four fields in one of the subcavities. The other three fields in this subcavity and all of the fields in the other subcavities are initially zero. In the simulation the QW gain is non-zero only in the central part of the QW epitaxial layer, with a constant positive value over an area the same size as the current aperture, which was assumed to have a diameter of $4\ \mu\text{m}$ in all cases, since only this area will be pumped by the injected carriers, neglecting a small diffusion of carriers in the lateral direction. The laterally non-uniform gain also implies that gain guiding is accounted for and may be effective in addition to the index guiding, as will be shown. To avoid that the laterally propagating field reaches the edge of the numerical window, which would lead to numerical errors, after propagation each field is multiplied by an attenuation function, which is equal to unity out to a large distance from the optical axis and then smoothly falls off with the radial distance to a value ~ 0.9 at the edge of the numerical window. This value does not have to be zero since the peripheral field will experience multiple damping as it passes through many subcavities before it is getting close to the edges of the numerical window; as can be seen in the inset of Fig. 3, showing the intracavity field profiles, even for the cavities with the strongest lateral leakage the field is zero at the edges of the numerical window.

When the cavity field has converged a thorough loss analysis is performed to find how much of the cavity field is lost due to each of the three optical loss sources: lateral loss (including diffraction loss), mirror outcoupling loss, and absorption loss. Since the laterally travelling field is completely attenuated before it reaches the edges of the numerical window, this implies that all the power of this field is consumed in the multiplication with the attenuating function. Since the fields before and after this multiplication are known one can easily calculate how much power is lost. This lateral loss power is related to the total energy in the cavity, which gives the cavity loss rate, normally expressed in ps^{-1} ; using the average speed of light in the cavity this value can be prorated as a loss per unit length (usually in units of cm^{-1}), which is probably the most common way of expressing loss and gain in lasers, and the one that will be used here. The outcoupling loss is similar to the lateral loss in the sense that this is also optical power that leaves the cavity, only here it occurs in the longitudinal direction – through the bottom and top mirrors, and is therefore more easily accounted for. One simply calculates the field that escapes from the bottom and top mirror, respectively, from the fields in the bottom and topmost subcavities, and the power they carry is the outcoupling power, from which the outcoupling loss per unit length is calculated as described above. Finally, the absorption loss is calculated from the absorbed optical power in each subcavity (which of course will be zero if there are no lossy materials in the subcavity), which is conceptually simple – it should be the power of the field at the starting interface of the subcavity minus the power of the field when it has reached the other interface, for both the left and right propagating fields. However, in layers with gain or absorption the optical power carried by a field is influenced by standing-wave effects, which complicates the relation between the optical field – which is the entity obtained in the cavity simulation – and the optical power. For details about how this is conveniently dealt with in a formulation based on fields defined at the subcavity boundaries, see the Appendix.

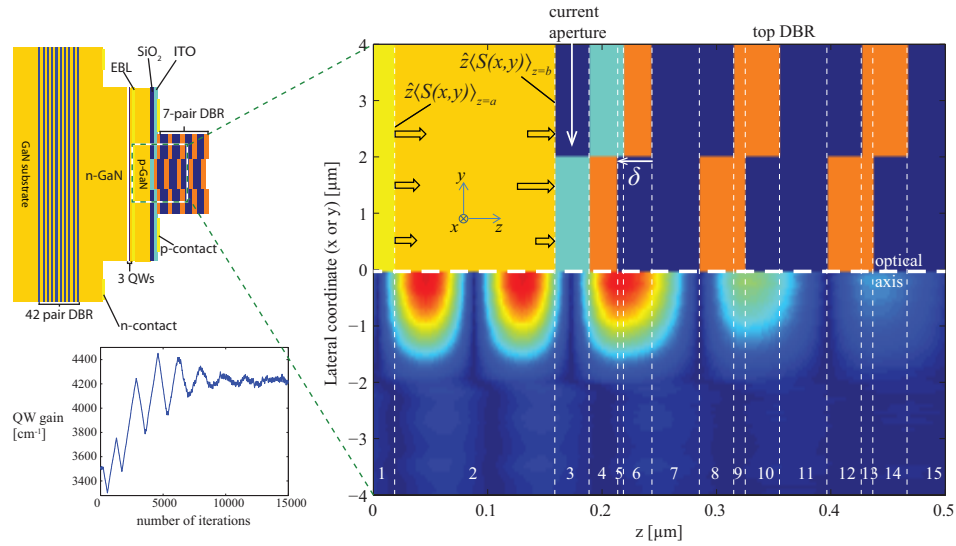


Fig. 1. Schematic of one simulated laser cavity (left) and composite figure showing the rotationally symmetric refractive index variation in a small part of the cavity (shown color-coded above the indicated optical axis) and the rotationally symmetric intracavity field for the fundamental mode. Different subcavities are labeled by integers and their boundaries are marked with vertical dashed lines. The inset shows an example of the convergence of the QW gain towards the threshold value in the iterative 3D cavity simulation algorithm. The symbols in subcavity 2 refer to the treatment in the Appendix.

After this the totally absorbed power in the cavity is simply calculated as the sum of absorbed power in all subcavities, which again is prorated per unit length.

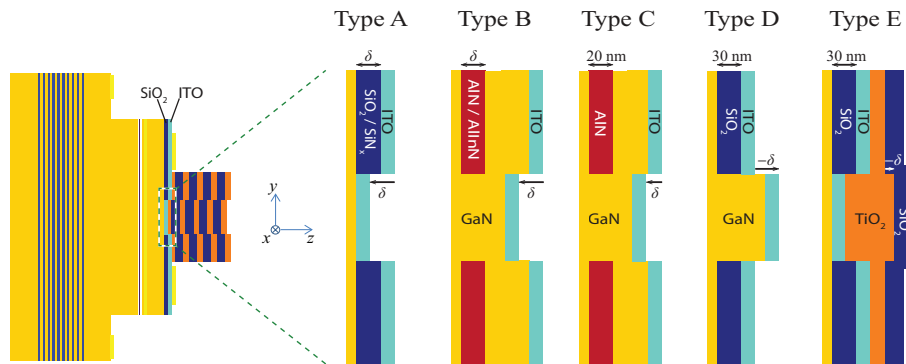


Fig. 2. Structures for the different types of current aperture realizations that have been analyzed.

3. Source-resolved optical loss in GaN-VCSELs for the fundamental mode

A number of cavity structures were analyzed, based on a proposed epitaxial design [16], with different suggested realizations of the current aperture with different thicknesses, and thus different values for the depression parameter δ . A generic representation of the different structures

Table 1. Investigated epitaxial layer structures and assumed material parameters.

Repeat	Material	Description	Thickness [nm]	Refractive index [-]	Absorption coefficient [cm^{-1}]
7×	TiO ₂	Top DBR	40.1	2.62	0
	SiO ₂	Top DBR	71.4	1.47	0
	TiO ₂	Top DBR	25	2.62	0
	ITO	Current spreader	30	2.10	1000
	SiN _x /SiO ₂ /AlN /AlInN	Peripheral part of current aperture	20–50	2.06 1.47 2.18 2.3	0
	GaN	Contact layer	140	2.49	10
	Al _{0.2} Ga _{0.8} N	Electron blocking layer (EBL)	20	2.42	0
	GaN	Contact layer	13	2.49	0
3×	In _{0.03} Ga _{0.97} N	QW barrier	6	2.68	0
	In _{0.1} Ga _{0.9} N	QW	5	3	0
	In _{0.03} Ga _{0.97} N	QW barrier	6	2.68	0
	GaN	Contact layer	946.6	2.49	10
42×	GaN	Bottom DBR	42.17	2.49	10
	Al _{0.8} In _{0.2} N	Bottom DBR	45.65	2.3	10
	GaN	Substrate		2.49	0

is shown in Fig. 2, and their entire layer structures are given in Table 1. We also considered structures where additional processing has been performed to decrease the structural depression and thus to increase the positive guiding; these structures are labeled Type C, D, and E in the figure. As indicated in the figure the current-blocking material in the current aperture was dielectric: SiN_x or SiO₂ as used in [1–5, 17], epitaxial AlN as considered in [18, 19], or regrown AlInN as studied in [20]. The calculated values for the material threshold gain in the QWs for all studied structures are shown in Fig. 3. These results are similar to the ones reported in [6], but with the addition of the two structures closest to $\Delta n_{eff} = 0$. Two things should be striking with this figure. First, how very accurately the effective index difference Δn_{eff} predicts the turning point from high threshold gain ($\Delta n_{eff} < 0$, i.e. antiguiding) to low threshold gain ($\Delta n_{eff} > 0$, i.e. guiding). Second, the abruptness of the transition from the highest to the lowest threshold gain is truly remarkable, occurring over just a few nanometers of structure change in the VCSEL cavity. Also shown in the figure are field profiles of the intracavity field near the QWs for a few cavities. Clearly, the central lobe, near the optical axis, looks much the same for both guided and antiguided cavities, only near $\Delta n_{eff} = 0$ is there a tendency for this lobe to be a little wider. On the other hand, the peripheral field is enhanced for the antiguiding cavities, which is an indication of their higher lateral loss, an effect which will be quantified in this section. Finally, in the figure the effective threshold gain is also indicated, i.e., the threshold gain in the QWs multiplied by the lateral confinement factor, the latter which is the overlap of the lateral field with the pumped QW area. The effective threshold gain can thus be viewed as the net QW gain that the cavity field experiences over its entire cross section, and will be used as a validation of the loss analysis.

To explain the features of the threshold gain curve, a thorough loss analysis was undertaken using the methods described in the previous section. Fig. 4 shows the three contributions to the

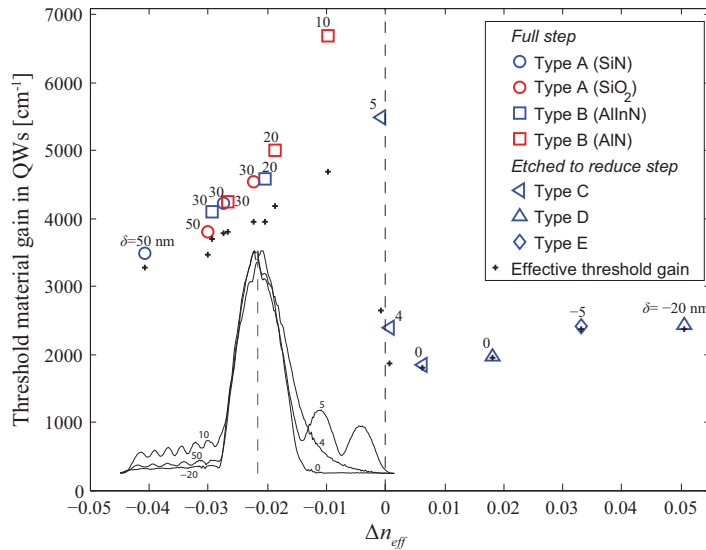


Fig. 3. Calculated threshold gain for the fundamental mode in the different laser cavities. The number at each marker is the structural depression parameter δ , and the plus sign below each marker indicates the threshold gain multiplied by the modal lateral overlap with the gain region. The inset shows six different mode profiles of the intracavity field amplitude at the position of the QWs, in the radial direction from the indicated optical axis plotted either to the left or right in the inset, for the displayed values of δ .

cavity loss. As expected, the absorption loss and the outcoupling loss do not vary much between the different cavity geometries, because they all have similar DBR mirrors and amount of lossy material in their cavities. The most interesting loss is the lateral loss, which is composed of two loss sources – diffraction loss, which is always present as a mostly small scattering loss in any device with a laterally varying index distribution, and the additional lateral leakage that occurs in the antiguided cavities. As can be seen, the lateral loss is very strongly dependent on cavity structure, being virtually zero for small positive guiding but dominant for moderate antiguiding. Further, when the positive guiding increases, the lateral loss increases somewhat because of increasing diffraction loss, which is expected. More unexpected is the fairly strong decrease of the lateral loss with increased antiguiding, in spite of the fact that also here the diffraction loss should increase. Because of the strong variation of the lateral loss the total loss also varies strongly. As a powerful check of the validity of the loss analysis, it is of particular interest to note that the total loss “curve” in Fig. 4 has exactly the same shape as the effective threshold gain in Fig. 3; they differ only by a constant because the loss is distributed in the cavity while the gain is the true material gain in the QWs. This precise correspondence is necessary for the customary gain-equals-loss relation for a laser at threshold to hold. For example, if standing wave effects had not been correctly accounted for in the calculation of the absorption loss, as outlined in the Appendix, the shape of the calculated total loss curve would be markedly different, indicating an error in the analysis.

4. Explaining the structural dependence of leakage loss

There are different ways to view the lateral leakage loss in antiguiding structures [21], but we have found that the approach taken by Hadley [14] is the most easily understood and is

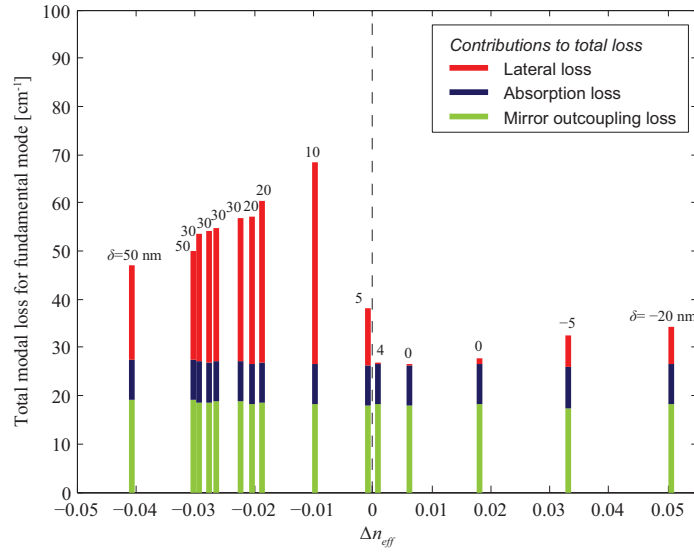


Fig. 4. Results of loss analysis for the fundamental mode in the studied VCSEL cavities.

directly supported by results extracted from our simulations. Hadley's idea is that for antiguided cavities, unlike guided, the peripheral cavity is at resonance for an oblique angle of propagation. In the antiguided cavity there is thus an efficient channel for lateral transport of optical power away from the central region near the optical axis. This is thus the mechanism responsible for the lateral leakage. The situation can be explained with the sketch in Fig. 5 This shows a simple, homogeneous hard-mirror model cavity with the depression, leading to antiguiding, being realized as a reduction of the cavity length by the distance δ_{cav} near the optical axis. For resonance of a longitudinally propagating field in the central part of the cavity there is the phase repetition condition, assuming that the two reflections from the hard mirrors in total add zero or 2π radians to the phase

$$k \cdot 2L = m_c \cdot 2\pi; \quad k = \frac{2\pi}{\lambda}, \quad (1)$$

where λ is the wavelength in the cavity medium and m_c is an integer. However, a field with the same oscillation frequency can also be resonant in the longer peripheral cavity if it propagates at an angle θ_p , since then the wavelength in the longitudinal direction also becomes longer, or, expressed as the resonance condition for the phase

$$k_{long} \cdot 2(L + \delta) = m_p \cdot 2\pi, \quad (2)$$

where $k_{long} = k \cdot \cos \theta_p$ and m_p is an integer. Assuming that δ_{cav} is small, it is reasonable to take $m_p = m_c$, which upon combining (1) and (2) gives

$$\cos \theta_p = \frac{L}{L + \delta_{cav}}. \quad (3)$$

Further, as indicated in the figure, from this peripheral lightwave some light will escape in the longitudinal direction since the cavity walls, i.e. the bottom and top mirrors, are not

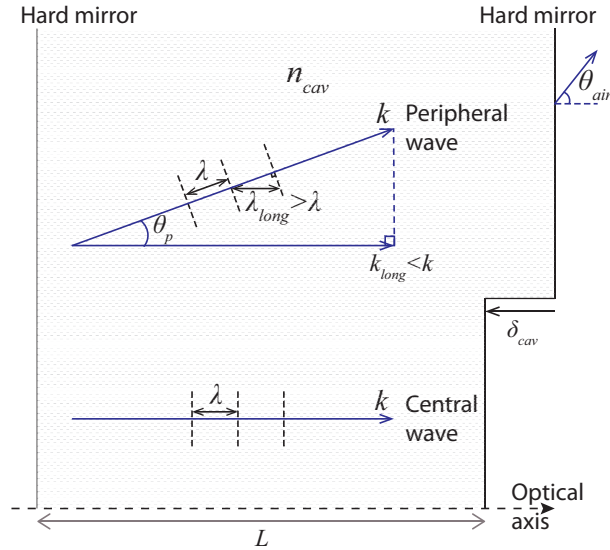


Fig. 5. A simplified model of the laser cavity as a hard-mirror model with a central depression, and filled with a homogeneous medium of refractive index n_{cav} . Dashed lines perpendicular to the k -vectors denote wavefronts.

perfectly reflecting, and be observable from outside the cavity. This light will have an angle of propagation, θ_{air} , which is simply given by Snell's law

$$\sin \theta_{air} = n_{cav} \sin \theta_p, \quad (4)$$

where n_{cav} is the refractive index of the cavity material between the hard mirrors. Obviously, the simulated cavities are far more complicated, but one could make a rough comparison with the above theory by perhaps assuming for the above parameters the values $L = 2 \mu\text{m}$, accounting for some field penetration into the DBR mirrors, and $n_{cav} = 2.49$, which is the refractive index of GaN. For the step δ_{cav} we use $\delta_{cav} = \delta - \delta_{offset}$, where δ is the physical step in the dielectric DBR profile, and δ_{offset} accounts for the fact that a certain step is needed to obtain zero guiding in our structures because the current aperture inherently provides some positive guiding. From Fig. 3, it is seen that it is reasonable to take $\delta_{offset} = 4 \text{ nm}$. With these values inserted in (3) and (4), a relation is obtained between δ and θ_{air} of the peripherally resonant field as shown by the solid curve in Fig. 6.

From our simulations the far-field intensity distributions for the antiguided cavities can also be extracted, some of which are shown as insets in the Fig. 6. The far-fields show a central lobe, which originates from the central cavity field, but also a "side lobe" - a distinct ring of light that indicates the existence of intracavity radiation with a preferred oblique angle of propagation, which is reasonable to attribute to the resonant wave in the peripheral cavity. It is also evident that the emission angle θ_{air} of this cone of light increases with δ . The figure shows the obtained values for θ_{air} for all simulated cavities with antiguiding. The qualitative agreement with the theoretical prediction for θ_{air} for the model cavity - the solid curve - makes it natural to assume that the simulated results indeed originate from a strong resonant wave in the peripheral cavity.

Finally, this picture for the lateral loss can also help us find a motivation for the decrease of the lateral leakage with stronger antiguiding, which was another notable feature of Fig. 4. We note that although the antiguided cavity opens a channel for efficient lateral transport of power,

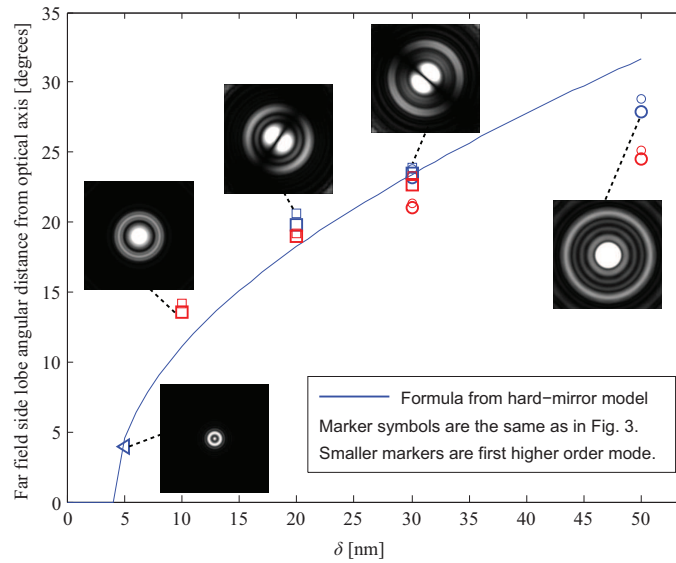


Fig. 6. Calculated propagation angle in air, measured from the optical axis, for the main side lobe in the output field distributions from antiguided cavities. All studied antiguided cavities are represented in this figure, both their fundamental and their first higher order modes (the latter does not exist for the cavity with the lowest δ). The solid line is the result of the resonance analysis for the simplified hard-mirror model. Insets show field distribution in the far-field for a few cases, with image saturation increasing with δ to be able to see the side lobe. All insets cover the same angular range (35 degrees from optical axis in the horizontal and vertical directions).

there will not be a significant lateral leakage unless also optical power is efficiently launched into the channel. The launch mechanism in this case should be the generation of obliquely propagating components of the central field as this field passes through the current aperture and the top DBR with its lateral profile, creating, in effect, multiple circular apertures of different refractive index in the central and peripheral parts. The net effect of all these apertures should be difficult to intuitively understand in detail, but since a single circular aperture produces a Bessel-shaped distribution of the scattered field as a function of launch angle, one might expect a fuzzy version of this distribution to be close to the real case; thus the launch of power is highest at small angles to the optical axis and less efficient for large angles. In the above analysis it was found that stronger antiguiding gives a more oblique angle of the resonant wave, and, from the discussion in this paragraph, thus a less efficient launch of power into that wave; this might thus at least partly explain the reduced lateral leakage for strong antiguiding.

5. Source-resolved optical loss in GaN-VCSELs for the first higher order mode

To simulate the first higher order mode in the cavity nothing is assumed about its field distribution other than it is orthogonal to the fundamental mode; it is also assumed that it has the lowest loss among the higher order modes. We therefore make use of $E_0(x,y)$, the converged fundamental mode solution, found in the analysis described in previous sections, at a certain cross section in the cavity. In the higher order mode simulations, in every iteration the actually obtained field in the same cross section, $E_{act}(x,y)$, contains a fraction κ of the fundamental

mode field

$$E_{act}(x,y) = \kappa E_0(x,y) + E_1(x,y) + E_{other}(x,y), \quad (5)$$

where $E_1(x,y)$ is the first higher order mode field and $E_{other}(x,y)$ is the field that contains neither fundamental nor first higher order mode fields. Multiplying (5) by the conjugate $E_0^*(x,y)$ and integrating over the cross section the last two terms vanish because of orthogonality, and the fundamental mode fraction becomes

$$\kappa = \frac{\iint_{x,y} E_{act}(x,y)E_0^*(x,y)dxdy}{\iint_{x,y} E_0(x,y)E_0^*(x,y)dxdy}. \quad (6)$$

The field content in the fundamental mode, $\kappa E_0(x,y)$, is now subtracted from the obtained field $E_{act}(x,y)$ and the resulting field is used for the starting field for the next iteration. This procedure is repeated in every iteration, but it is sufficient to do the removal of the fundamental mode in one of the subcavities, this corresponds to a very high artificial loss for the fundamental mode in that subcavity that will strongly suppress the mode in the entire cavity.

In all other respects the simulations are done as for the fundamental mode simulation, and the same cavities were studied. For antiguiding cavities, the resonance for an obliquely propagating wave in the peripheral cavity only depends on the cavity structure, so one expects that the propagation angle of the laterally leaking wave is independent on the mode order. As shown in Fig. 6, this can be clearly seen in the far-field intensity patterns, where the side lobes are positioned at the same angle from the optical axis for the fundamental and first higher order mode. However, the intensity of the side lobes is different since the angular spectrum of the in-

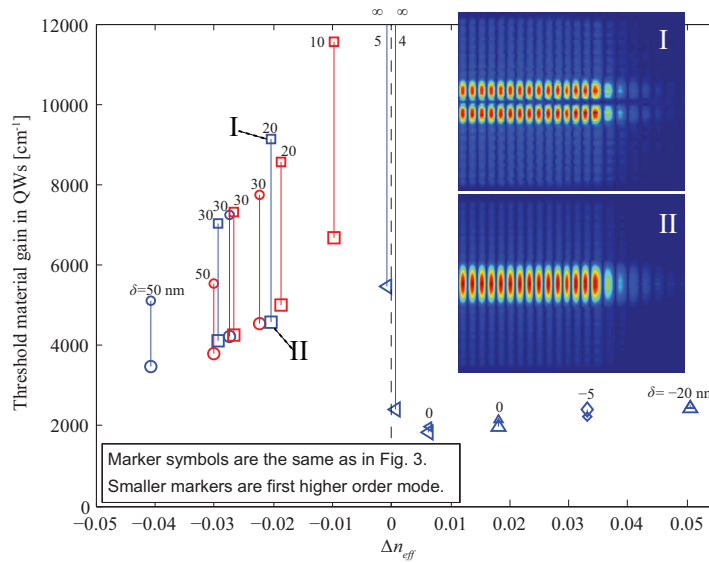


Fig. 7. Calculated threshold gain for the first higher order mode. The threshold gain for the fundamental mode from Fig. 3 is also plotted here for convenient comparison (larger markers of same shape and color). The vertical lines connecting the threshold gain values for the fundamental and first higher order mode for the same cavity thus indicate the modal discrimination of this cavity. Insets show cross sections of the intracavity fields above the bottom DBR in the indicated cavity for the fundamental and higher order mode.

tracavity field is different. In general the higher order mode contains more field propagating at large angles, including the oblique angle corresponding to the peripheral resonance, and should therefore have a larger leakage loss than the fundamental mode, as will also be shown in the following.

The obtained QW threshold gain values for the first higher order mode are shown in Fig. 7 and compared with those for the fundamental mode. It can first be noted that for the cavities closest to zero guiding the higher order mode does not even exist in the cavity; for these cases there was no stable solution for the higher order cavity field even at very high QW gain values. Away from the region with almost zero guiding, for positive guiding there is evidently very little mode discrimination since the markers for fundamental and higher order modes are almost on top of each other. For antiguiding, on the other hand, there is a strong mode discriminating effect, with threshold gain values up to almost twice those of the fundamental mode.

To analyze the loss, the loss contributions are plotted in Fig. 8. Comparing with Fig. 4, which was deliberately drawn with the same scaling on the vertical axis to facilitate comparison, one immediately sees that the main difference in the loss is the lateral loss for antiguided cavities, which is much larger for the higher order mode. In relative terms, the percentages given in Fig. 8 show that the lateral loss is roughly 50–100% higher for the first higher order mode than for the fundamental mode in the antiguided cavities. Although this is significant, it is still far lower than in some formulas used as a rule-of-thumb for other antiguided laser cavities where the lateral loss is assumed to have an $(m + 1)^2$ -dependence, where $m = 0$ for the fundamental mode and $m = 1$ for the first higher order mode [21, 22]; obviously, these formulas predict that the lateral loss for the first higher order mode should be $\sim 300\%$ larger than for the fundamental mode.

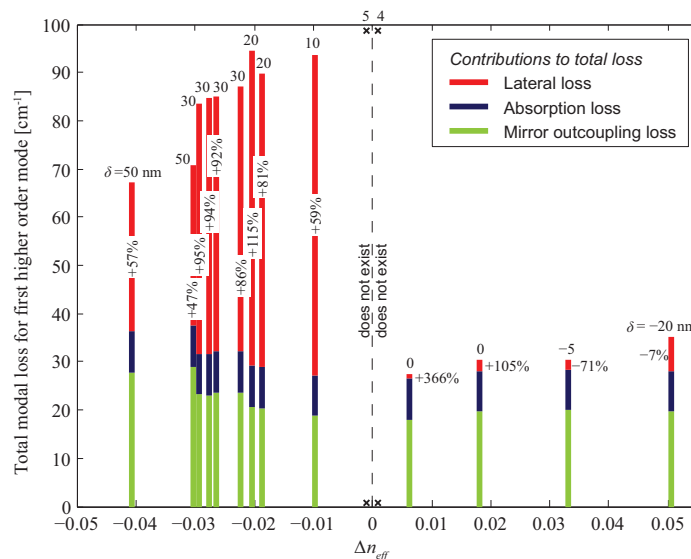


Fig. 8. Results of loss analysis for the first higher order mode in the studied VCSEL cavities. The indicated percentages are the relative change in the lateral loss compared to the case for the fundamental mode.

Looking closely in the figure, for the strongest antiguided cavities one can also see that the mirror outcoupling loss is higher for the higher order mode than for the fundamental mode. This is caused by an increase in the outcoupling through the top mirror; evidently, the reflectance of

the higher order mode suffers more from the step structure in the DBR. On the other hand, the absorption loss is virtually independent of the mode order, as expected.

For the cavities with positive guiding the loss is virtually independent of mode order, as could be anticipated from the similarity in threshold gain values. For the two cases with Δn_{eff} up to ~ 0.02 , the large relative increase in the lateral loss shown in Fig. 8 is a numerical artifact, since it is compared to a very small lateral loss for the fundamental order mode, and since the fields for these weakly guided higher order modes have tails that extend out to the absorption region near the borders of the numerical window, which means that they suffer an artificial extra loss accounted for as lateral loss. For stronger positive guiding it is in fact observed that the lateral loss is lower for the first higher order mode, which for the cavity with $\Delta n_{eff} = 0.033$ even leads to a slightly lower threshold gain for the first higher order mode than for the fundamental mode. This also means that the fundamental mode simulations for this particular case could not be performed with a random starting field, which would eventually converge to the first higher order mode, but started from a rotationally symmetric Gaussian field distribution.

6. Conclusions

We have analyzed the contributions from the three loss sources – outcoupling (mirror) loss, material absorption and lateral loss – to the total loss in proposed GaN-based laser microcavities for blue emission. It was found that the lateral loss was extremely sensitive to details in the realization of the current aperture and top mirror. This occurs because small structural changes slightly change the guiding strength that may lead to the lateral loss changing character from what might be called diffraction loss to lateral leakage, or vice versa. Diffraction loss is the normal lateral loss in a (positively) guided cavity and gives only a small contribution. Lateral leakage, on the other hand, is the detrimental lateral loss that occurs as soon as the cavity becomes antiguided. It was argued that entering the antiguided region opens an efficient channel for light to escape in the radial direction since the peripheral part of the cavity becomes resonant for light with a certain propagation angle; this was supported by calculated far-fields from different cavities.

By suppressing the fundamental mode, we further analyzed the losses for the first higher order mode in the cavities. They were similar to those of the fundamental mode with the important exception of the lateral loss for antiguided cavities, which was higher by typically 50–100%. Although this is a significant increase, it is still lower than the increase by a factor of ~ 4 that is predicted from simple analytical formulas. The suggested deliberate use of VCSELs operating well into the antiguided region, utilizing their inherent discrimination against higher order modes, may thus be less advantageous than previously anticipated.

Finally, it should be mentioned that in physical devices there are non-ideal effects that also contribute to the guiding, the most important being the higher temperature in the central part of the device, which adds (positive) guiding because the refractive index of a semiconductor increases with temperature (thermal lensing). It was also assumed that the topography near the current aperture is precisely maintained in all layers above, while in reality there is an increasing smoothing of the profile step towards the air interface of the top DBR mirror. In a specific case such effects might be readily included in the existing simulation tool after having established the actual top layer structure by, e.g., inspection by electron microscopy. It can be anticipated, though, that this will not have too dramatic effect because of the limited field penetration into the top DBR mirror. On the other hand, fabrication imperfections in parts of the cavity where the field is high may give significant unintentional contributions to the guiding that can be either positive or negative. For instance, many etching or sputtering techniques give unwanted (re-)deposition of material, giving rise to ridges or other topological formations in the layers close to the current aperture. Although such a ridge may be only on the order of 10 nm thick,

simulations with the program used throughout this work show that it can lead to antiguiding, triggering an increased lateral loss by orders of magnitude, causing a strong increase of the threshold QW gain. Even if one does not perform the full 3D analysis described here, it makes sense to test a suggested cavity structure with the simpler 2D effective index method to obtain the effective index difference Δn_{eff} . If this value is close to zero one might consider to slightly change the structure to move further into the positive guiding region where the consequences of a small, uncontrolled change in guiding strength are much less dramatic.

Appendix: Generated/absorbed power in a subcavity calculated from fields at the subcavity boundary

The BPM method considers a left- and a right-propagating field. It would, therefore, seem natural to also assign a left- and right-propagating intensity or power flux. This is not a problem as long as the propagation occurs in a medium without gain or loss. However, in a gainy or lossy medium the power flux in the right and left directions, in whatever way they may be defined, become coupled and exchange energy with each other – this is the standing wave effect. Therefore, one should avoid the concept of right- and left propagating intensity, and only consider the net flux of power in any cross section. In this appendix we derive an expression that yields the net power flux across a subcavity boundary, and consequently the absorbed or generated power in the subcavity, in the most straightforward way from the optical fields at the boundary.

The net flux of power of a field propagating in the positive and negative z -direction in a point $\tilde{z} = 0$ in a local coordinate system, with the origin $\tilde{z} = 0$ being located infinitely close to the subcavity boundary but inside the material of the subcavity under study, is given by the time average of the Poynting vector \bar{S}

$$\bar{S} = (\bar{E}^{\rightarrow} + \bar{E}^{\leftarrow}) \times (\bar{H}^{\rightarrow} + \bar{H}^{\leftarrow}) = \bar{E}^{\rightarrow} \times \bar{H}^{\rightarrow} + \bar{E}^{\leftarrow} \times \bar{H}^{\leftarrow} + \bar{E}^{\rightarrow} \times \bar{H}^{\leftarrow} + \bar{E}^{\leftarrow} \times \bar{H}^{\rightarrow}, \quad (7)$$

evaluated at $\tilde{z} = 0$, where \bar{E}^{\rightarrow} and \bar{H}^{\rightarrow} are the right- and left- propagating electric and magnetic fields, respectively. Locally around $\tilde{z} = 0$ the nearly one-dimensionally propagating fields can be described with plane wave expressions

$$\begin{aligned} \bar{E}^{\rightarrow} &= \hat{x}E_0^{\rightarrow} e^{\gamma \tilde{z}} \cos(k\tilde{z} - \omega t) & \bar{E}^{\leftarrow} &= \hat{x}E_0^{\leftarrow} e^{-\gamma \tilde{z}} \cos(-k\tilde{z} - \omega t + \Delta\varphi) \\ \bar{H}^{\rightarrow} &= \hat{y}H_0^{\rightarrow} e^{\gamma \tilde{z}} \cos(k\tilde{z} - \omega t + \varphi_H) & \bar{H}^{\leftarrow} &= \hat{y}H_0^{\leftarrow} e^{-\gamma \tilde{z}} \cos(-k\tilde{z} - \omega t + \Delta\varphi + \varphi_H), \end{aligned} \quad (8)$$

where γ is the power gain (negative for loss) per unit length in the material, E_0^{\rightarrow} and H_0^{\rightarrow} are constants, φ_H is the phase lag between the electric and magnetic field that occurs in gainy/lossy materials, and $\Delta\varphi$ is the phase difference between right and left propagating electric fields at $\tilde{z} = 0$. By inserting (8) into (7) and carrying out the time average one obtains the desired net flux of power (net intensity) in the z -direction at $\tilde{z} = 0$

$$\begin{aligned} \langle \bar{S} \rangle &= \hat{z} \frac{1}{2} \{ E_0^{\rightarrow} H_0^{\rightarrow} \cos \varphi_H + E_0^{\leftarrow} H_0^{\leftarrow} \cos \varphi_H + E_0^{\rightarrow} H_0^{\leftarrow} (\cos \varphi_H \cos \Delta\varphi - \sin \varphi_H \sin \Delta\varphi) + \\ &E_0^{\leftarrow} H_0^{\rightarrow} (\cos \varphi_H \cos \Delta\varphi + \sin \varphi_H \sin \Delta\varphi) \} \equiv \hat{z} \langle S \rangle. \end{aligned} \quad (9)$$

To remove the unknown phase lag φ_H and magnetic fields from (9) the right and left propagating fields in (8) are respectively inserted into the first Maxwell equation in one dimension

$$\frac{\partial E_x}{\partial \tilde{z}} = -\mu_0 \frac{\partial H_y}{\partial t}, \quad (10)$$

where the subscripts on the fields denote the components of the vectors. This gives us the relations

$$\begin{aligned} H_0^{\rightarrow} \cos \varphi_H &= E_0^{\rightarrow} \frac{k}{\mu_0 \omega} & H_0^{\leftarrow} \cos \varphi_H &= -E_0^{\leftarrow} \frac{k}{\mu_0 \omega} \\ H_0^{\rightarrow} \sin \varphi_H &= -E_0^{\rightarrow} \frac{\gamma}{2\mu_0 \omega} & H_0^{\leftarrow} \sin \varphi_H &= E_0^{\leftarrow} \frac{\gamma}{2\mu_0 \omega}. \end{aligned} \quad (11)$$

Inserting (11) into (9) gives us the simple expression

$$\langle S \rangle = \frac{1}{2\mu_0 c_0} \{ (E_0^{\rightarrow})^2 n - (E_0^{\leftarrow})^2 n + 2E_0^{\rightarrow} E_0^{\leftarrow} n'' \sin \Delta\phi \}, \quad (12)$$

where $k = nk_0 = \frac{n\omega}{c_0}$ was used, where n is the (real part of) the refractive index of the material in $\tilde{z} = 0$, and $\gamma = -2n'' \frac{\omega}{c_0}$, where n'' is the imaginary part of the refractive index. Evidently, the last term in (12) is responsible for the standing wave effect, depending on the phase relation $\Delta\phi$ between the counterpropagating fields. In a material without gain/loss, $n'' = 0$, so the power flux can then be viewed as being composed of independent contributions from the right and left propagating field. Finally, one integrates (12) over the cross section, i.e. in the (x, y) -plane, using the slowly varying values of $E_0^{\rightarrow}(x, y)$, $E_0^{\leftarrow}(x, y)$, and $\Delta\phi(x, y)$, which yields the net optical power transported through the cross section. To obtain the power generated in a subcavity, P_{sc} , one simply sums the outgoing power at the two cross sections, at $z = a$ and $z = b$, that constitute the boundaries of the subcavity

$$P_{sc} = \iint \{ \langle S(x, y) \rangle_{z=b} \} dx dy + \iint \{ -\langle S(x, y) \rangle_{z=a} \} dx dy, \quad (13)$$

where $b > a$ is assumed and the minus sign comes from the outward direction from the subcavity being in the negative z -direction at the left boundary $z = a$, see Fig. 1 where this is illustrated for the subcavity labeled '2'. Since P_{sc} defined in this way yields the generated power, $P_{sc} > 0$ in the subcavities containing the QWs, and $P_{sc} < 0$ in subcavities containing lossy material where the magnitude of P_{sc} is the absorbed power in the material.

Acknowledgments

This work was funded by the Swedish Research Council (VR).